SPECIAL TOPIC

Waves in planetary dynamos

K. Hori[1] · A. Nilsson[2] · S. M. Tobias[3]

Abstract

This Special Topic focuses on magnetohydrodynamic (MHD) processes in the deep interiors of planets, in which their fluid dynamos are in operation. The dynamo-generated, global, magnetic fields provide a background for our solar-terrestrial environment. Probing the processes within the dynamos is a significant theoretical and computational challenge and any window into interior dynamics greatly increases our understanding. Such a window is provided by exploring rapid dynamics, particularly MHD waves about the dynamo-defined basic state. This field is the subject of current attention as geophysical observations and numerical modellings advance. We here pay particular attention to torsional Alfvén waves/oscillations and magnetic Rossby waves, which may be regarded as typical axisymmetric and nonaxisymmetric modes, respectively, amongst a wide variety of wave classes of rapidly rotating MHD fluids. The excitation of those waves has been evidenced for the Earth — whilst their presence has also been suggested for Jupiter. We shall overview their dynamics, summarise our current understanding, and give open questions for future perspectives.

Keywords MHD · Rotating fluids · Waves · Dynamos · Planets

A. Nilsson and S. M. Tobias have contributed equally to this work.

✉ K. Hori
khori@people.kobe-u.ac.jp

A. Nilsson
andreas.nilsson@geol.lu.se

S. M. Tobias
s.m.tobias@leeds.ac.uk

[1] Graduate School of System Informatics, Kobe University, Rokkodai 1-1, Nada, Kobe 657-8501, Japan

[2] Department of Geology, Lund University, Sölvegatan 12, Lund 22362, Sweden

[3] Department of Applied Mathematics, University of Leeds, Woodhouse Lane, Leeds LS2 9JT, UK

1 Introduction

1.1 Some background on magnetic field

Our planet has a global magnetic field that is predominantly an axial dipole nearly aligned with the geographical poles. As this field shapes part of the solar-terrestrial environment it is of great interest in the Special Topics. The large-scale structure of the magnetic field, including the dipole, has its origin in the interior below the surface (Fig. 1a). The field has persisted for at least 3.4 billion years (Tarduno et al. 2010); however it is not the result of a permanent magnet — it exhibits variations on many different timescales. For example the dipole component has occasionally weakened and reversed its polarity on intervals of the order 10^5–10^7 years (e.g., Cande and Kent 1995; Biggin et al. 2012), whilst other components drift westwardly on periods of the order 10^2–10^3 years (e.g., Bullard et al. 1950; Nilsson et al. 2020). Moreover timeseries of the field observations repeatedly experience abrupt changes, called jerks, on intervals of the order 10^0–10^1 years (e.g., Courtillot and Le Mouël 1984; Mandea et al. 2010). All of these variations with an internal origin are referred to as geomagnetic secular variation.

Dynamo action is believed to operate in the interior region termed the fluid outer core, which is located below $\sim 54.6\%$ of the planet's radius R_E (hereafter we denote $r_{core} \sim 0.546 R_E$). The fluid outer core is made of liquid iron and some lighter chemical components. The origin of the dynamo process lies in the motion of the electrically conducting fluid, this induces an electric current within the region, and that maintains a magnetic field. The detailed processes have not entirely been solved, owing to their theoretical and computational complexity; the fluid dynamics therein is likely dominated by the planet's rotation and magnetic field, rather than inertia and viscosity (as we see below). Geodynamo theory therefore necessitates the understanding of the MHD of rapidly rotating fluids. In that respect the research area shares a lot with the atmospheric and oceanic dynamics, and so may be regarded as part of "geophysical fluid dynamics".

Some other planets are found to possess global magnetic fields that are also thought to be generated through dynamo mechanisms (see reviews, e.g., by Stevenson (2010); Jones (2011); Schubert and Soderlund (2011); and references therein). It
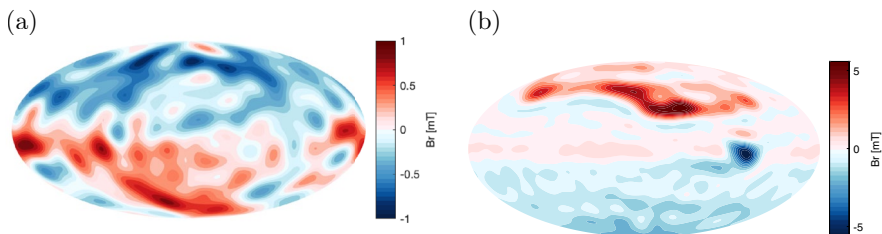

Fig. 1 **a** Earth's magnetic field in 2020 at $r = 0.546\,R_E = r_{core}$, the top of the fluid core (reproduced from Finlay et al. (2020) with spherical harmonics of degree up to 13). **b** Jupiter's magnetic field in 2016–2021 at $r = 0.85\,R_J$, supposed to be a top of the metallic hydrogen region (reproduced from Connerney et al. (2022) with spherical harmonics of degree up to 18)

is however still unclear where in those planets dynamos operate; the internal structures of planets other than Earth are not well determined. Jupiter, for example, is a gaseous planet mostly made of hydrogen and helium and has the strongest planetary magnetic field (Fig. 1b). The gas giant's dynamo is likely active in the metallic hydrogen envelope; though the exact location is uncertain. Indeed the NASA Juno spacecraft (e.g., Bolton et al. 2017; Stevenson 2020) has been orbiting the planet to determine the internal structure, and is producing evidences that the conductive region likely spans up to $\sim 80 - 90\%$ of the planet's nominal radius R_J. Recall that Earth's dynamo sits deep inside and is masked by the rocky mantle, which acts as an insulator, screening the small-scale structure of the magnetic field. Exploring the fields of other planets, particularly Jupiter where the conducting region is not screened as effectively, could provide us with deeper knowledge about the operation of natural dynamos (Jones and Holme 2017).

1.2 A brief introduction to dynamo theory

The early foundations of dynamo theory were made over a century ago and progress involved advances in applied mathematics and fluid dynamics. Early outcomes involved the demonstration of multiple anti-dynamo theorems that limit the structure of dynamo-generated magnetic fields and the flows that generate them; for example Cowling's Theorem states that a purely axisymmetric magnetic field cannot be generated by dynamo action, whilst Zel'dovich's theorem maintains that a purely two dimensional fluid motion cannot drive a dynamo; we refer to Moffatt (1978); Roberts (1994); Dormy and Soward (2007); and Tobias (2021) for reviews. Those early works unraveled key elements for dynamo action, one of which is the necessity of interactions between toroidal and poloidal components of the magnetic field, which are defined from a decomposition of the field based on the solenoidal condition. Mean-field theory, where the interacting terms, e.g., the electromotive force arising from turbulent interactions are modelled or parameterised, yields steady or oscillatory solutions, dependent on the relative strength of interactions; there is yet a wealth of theory describing limitations on the form and applicability of the interaction terms (Moffatt 1978; Hori and Yoshida 2008; Tobias 2021). This theory yields the basics of how a global magnetic field can be maintained and also mechanisms for periodic cycles.

In the age of computational physics and geophysics, numerical investigations have been pursued to solve the self-consistent dynamo problem, where the magnetic field is destabilised and sustained by fluid motions that are driven, for example, by buoyancy, and acts back on the flows that are driving it. Buoyancy-driven convection is thought to be a primary source of planetary dynamos, including Earth and Jupiter, where the planet's thermal evolution is active. Convective instability has been greatly studied, alongside the dynamo instability and we refer to Jones (2015) for reviews. Numerical dynamos driven by convection in spherical shells first succeeded in the 1990s in reproducing the generation of global magnetic field and its polarity reversals (Glatzmaier and Roberts 1995; Kageyama and Sato 1995). This was followed by many numerical simulations (see reviews by Christensen and Wicht (2015) and Jones (2011)) to reveal their scaling properties (e.g., Christensen

and Aubert 2006; Davidson 2013), and to replicate individual planets and moons including gaseous planets (Jones 2014; Gastine et al. 2014b). Owing to the large separation of timescales that are relevant to the dynamics of Earth's magnetic field, early geodynamo simulations suffered from an issue such that their self-generated magnetic fields did not represent the physical regime expected to pertain to Earth's interior, called the magnetostrophic regime (see below). However recently a consensus is building that simulations are beginning to enter the relevant regime (e.g., Yadav et al. 2016; Dormy 2016; Schaeffer et al. 2017; Aubert et al. 2017); there are still ongoing debates, for example, on the existence of strong-/weak- field branches (Dormy 2016) and on the lengthscale-/spatial- dependence of the force balance (Schwaiger et al. 2019), i.e., on what scales the viscous balances pertain.

1.3 Detailed observations

Concurrently, geophysical observations together with data modelling techniques have been advancing enormously. Ground-based measurements and archaeological/ sedimentary records have been analysed to enable the recovery of the field evolution for past few thousand years down to a spatial wavelength of 72° (e.g., Korte et al. 2011; Nilsson et al. 2014; Hellio and Gillet 2018). This has enabled the description, for example, of millennial-scale high-latitude westward drifts (Nilsson et al. 2020) and spikes (Davies and Constable 2017). Moreover, today's satellite missions, including the Swarm mission, have mapped in detail the variations of the present-day geomagnetic field. Global models based on such measurements have established detailed descriptions of the secular "variation", defined by the temporal derivative of the interior-origin field, and also the "acceleration" (the second derivative) arising from the fluid core (e.g., Finlay et al. 2020). This analysis has led to the discovery of rapid dynamics, such as the several-year westward drift near the equator (Chulliat et al. 2015) and the polar jet (Livermore et al. 2017).

It has also enabled inversions to describe the fluid motion over the dynamo region: such an outcome is called the "core flow model". We refer to Holme (2015) for a review. A prominent feature found by those inversions is a single anticyclonic vortex, sometimes referred to as the eccentric gyre (Fig. 2) (e.g., Pais and Jault 2008), which has likely persisted for more than 100 years, although some fluctuations are observed. Currently data assimilation, where observations are combined with theoretical dynamo models, is becoming a common technique to provide core flow information (e.g., Fournier et al. 2011; Gillet et al. 2019). It could therefore also be quite natural to construct core flow models for other planets. This has, in part, been attempted for Jupiter, in which the magnetic secular variation was realised in early missions (e.g., Ridley and Holme 2016); now the Juno mission is going to provide more details (Moore et al. 2019; Bloxham et al. 2022).

1.4 Waves: the focus of the Special Topics

With motivation from the advances described above, we here focus on MHD waves in planetary dynamos. They seemingly give a framework for thinking about
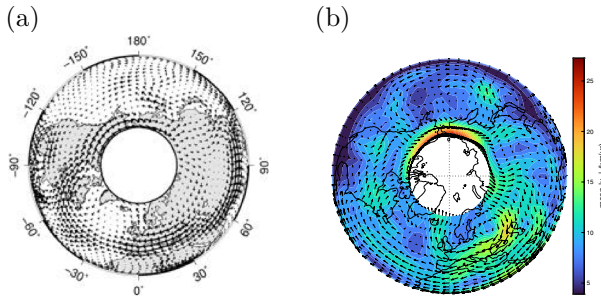
Fig. 2 Core flows inverted from geomagnetic secular variation. Arrows represent velocity, of the order 10^{-3} m/s, in the equatorial plane. Averages **a** over 1840–1990, adapted from Pais et al. (2015), and **b** over 1890–2010, reproduced from Gillet et al. (2019)

the secular variation/acceleration and rapid dynamics, in contrast to convection or dynamo action, in which diffusion matters and for which a typical timescale is of the order of 10^5 years and more in Earth, for example. Indeed, exploring waves is highly beneficial as their properties could yield information about the interior that is inaccessible through direct observations. The related science of seismology has successfully scanned the elastic structure of our terrestrial planet, however is hindered from probing the fluid dynamo region in detail. An alternative investigation, utlising MHD waves could potentially visualise this, sensing the hydromagnetic properties such as the poloidal and toroidal component of the magnetic field; in some sense there is an analogy with the study of the properties of the solar atmosphere using "coronal seismology".

We give a mathematical formulation to describe our problem below. We begin with the fluid (MHD) description. We here consider anelastic fluids where the Lantz-Braginsky-Roberts-Jones formalism (e.g., Braginsky and Roberts 1995; Jones et al. 2009, 2011) is adopted, which enables the inclusion of stratification for subsonic flows. We assume that the equilibrium state is close to adiabatic, well-mixed, and hydrostatic with density $\bar{\rho}$. The velocity of interest $\boldsymbol{u}$ is subsonic (cf. the sound/seismic waves of the order 10^4 m/s in Earth) so that the continuity equation becomes

$$\nabla \cdot \bar{\rho}\boldsymbol{u} = 0 \ . \tag{1}$$

For simplicity, we assume that the basic state $\bar{\rho}$ depends solely on spherical radius, r. Focusing on the dynamics whose characteristic timescales are shorter than the diffusion times (see above), we then consider the momentum equation

$$\bar{\rho}\left[\frac{\partial \boldsymbol{u}}{\partial t} + (\boldsymbol{u} \cdot \nabla)\boldsymbol{u} + 2\boldsymbol{\Omega} \times \boldsymbol{u}\right] = -\nabla p' + \boldsymbol{j} \times \boldsymbol{B} \ , \tag{2}$$

where $\boldsymbol{\Omega}$ is the rotational angular velocity, $\boldsymbol{j}$ is the current density, $\boldsymbol{B}$ is the magnetic field, and p' is a reduced pressure incorporating the gravitational potential. The induction equation for magnetic field $\boldsymbol{B}$ is given by

$$\frac{\partial \boldsymbol{B}}{\partial t} + \boldsymbol{u} \cdot \nabla \boldsymbol{B} = \boldsymbol{B} \cdot \nabla \boldsymbol{u} - (\nabla \cdot \boldsymbol{u})\boldsymbol{B} \tag{3}$$

where the MHD approximation has been made in the non-relativistic Maxwell equations and combined with Ohm's law for a moving conductor. Of course the magnetic field is solenoidal. The density variation in Earth's fluid core is likely less than 20%, so for models of the Earth $\bar{\rho}$ in those equations may be assumed to be constant and the theory reduces to the incompressible, Boussinesq equations of MHD. In Jupiter, by contrast, the density varies by orders of magnitude. Wave solutions are obtained as fluctuations about a basic (or background) state of density, flow, and magnetic field. Conversely, measurement of wave properties such as frequencies could allow the inference of physical quantities of the background media.

Here we note the above equations give an ideal framework to examine the wave dynamics particularly and ought to be distinguished from those for dynamo action and convection (see above). Current planetary dynamo simulations, as discussed in Sect. 1.2), mostly solve equations including buoyancy, viscosity and diffusion. Below we shall adopt those simulations to examine to what extent our diffusion-free, buoyancy-free framework could be beneficial.

We first consider some dimensionless parameters to define the dynamical regime of interest. A key parameter is the Rossby number $Ro = U/L\Omega$, where U and L are a typical velocity and lengthscale respectively; this quantifies the relative strength of the inertia to the Coriolis force in the momentum equation. In Earth's fluid core $Ro \sim 1 \times 10^{-5}$, provided the speed U is represented by the slow inverted core flows of $\sim 10^{-3}$ m/s and $L \sim 10^6$ m (a global scale), and $\Omega \sim 7.3 \times 10^{-5}$ s^{-1}. Jupiter's metallic region likely has $Ro \sim 6 \times 10^{-6}$ for $U \sim 10^{-2}$ m/s, $L \sim 10^7$ m, and $\Omega \sim 1.8 \times 10^{-4}$ s^{-1}. Those suggest a minor role of the inertia, compared with rotation — at least on large lengthscales (and even for quite small scales!). For hydrodynamic flows, the fluid motion in those situations may be expected to be two dimensional (invariant in the direction of rotation), via the Proudman-Taylor theorem; such a mode is often called geostrophic, where the Coriolis force is largely balanced by a pressure gradient. In the presence of magnetic field, it is possible to have a force balance where the Coriolis, Lorentz, and pressure gradient forces are important; this is called a magnetostrophic balance and we stress that different balances may be found at different scales. These balances will have a significant impact on the dynamics, not only wave dynamics but also that relating to convection and dynamo action. Overviewing all aspects is beyond the scope of the present paper. Here we just comment that waves will be capable of diagnosing such a dynamo state and focus on that aspect.

Analysis of MHD waves in rotating fluids dates back to the 1950-60s (e.g., Lehnert 1954; Hide 1966; Malkus 1967; Braginsky 1967; Acheson and Hide 1973). Those ideas were examined further, as geomagnetic modelling and core flow inversions were upgraded (e.g., Zatman and Bloxham 1997; Finlay and Jackson 2003). We are in an exciting era, where new data and tools are increasingly arriving (Sect. 1.3) and this has led to a re-invigoration of theoretical investigations, as well as observational explorations (e.g., Gillet et al. 2010; Finlay et al. 2010; Buffett 2014). This is intrinsically

linked to — and sheds light on — geophysical issues such as the existence of a thin stably-stratified layer atop Earth's fluid core, overlying the main dynamo region. Waves in such a stratified environment were termed Magnetic-Archimedes-Coriolis (MAC) waves (Braginsky 1967). This contrasts with those in unstratified situations, where such waves are referred to Magnetic-Coriolis (MC) waves.

What makes the subject attractive is the wide variety of different wave classes. This arises from the combination of MHD, rotation, and stratification in some cases; all of which singly are classic research areas in fluid dynamics — however their combination yields a unique physics. (This could be analogous to the situation for plasma physicists, who seem to enjoy another blend with particles, compressibility, and so on.) The complex situation is manifested even for linear waves where classification itself is an ongoing topic of current research; spherical geometry and the morphology of the basic magnetic field makes the problems distinctive. For example, a comprehensive investigation in a spherical, magnetised, shallow-water system was recently made by Márquez-Artavia et al. (2017), where a simple background field was assumed; here recall an equivalent analysis in the hydrodynamic case was made by Longuet-Higgins (1968). Further works are finding peculiar eigenmodes such as equatorially or polarly trapped ones (e.g., Buffett and Matsui 2019; Nakashima 2020; Chi-Durán et al. 2021).

Below we overview our recent work, linking to the broader subject. The focus here is two wave classes, torsional Alfvén waves (Sect. 2) and magnetic Rossby waves (Sect. 3). They are characteristic axisymmetric and nonaxisymmetric MC modes respectively that can be excited within dynamo regions. Their dynamics are dictated by the magnetostrophic balance in rapidly-rotating systems. We examine the fundamentals of such waves and exemplify their role in Earth and Jupiter. This will give us the physical basis to consider further complications, such as the introduction of stratification to the waves.

2 Torsional Alfvén waves

We initially examine an axisymmetric mode, termed a torsional oscillation or torsional Alfvén waves. We begin with some fundamentals of the theory (Sect. 2.1), and then examine their importance for Earth (Sect. 2.2); we than provide a re-examination in updated geomagnetic datasets (Sect. 2.3) and potential implications in Jupiter (Sect. 2.4).

2.1 Fundamentals

We here outline the basic theory, following the literature (e.g., Braginsky 1970; Roberts and Aurnou 2012; Jault and Finlay 2015; Hori et al. 2019). Our basic equation is the azimuthal component of (2) in cylindrical polar coordinates (s, ϕ, z) where the z coordinate is supposed parallel to the rotation axis $\boldsymbol{\Omega}$. To seek the axisymmetric two-dimensional component, we take the integral over cylindrical surfaces along the rotational axis to yield

$$\frac{\partial}{\partial t}\langle \overline{\rho\, u_\phi}\rangle = -\left\langle \overline{\hat{e}_\phi \cdot (\nabla \cdot \overline{\rho uu})}\right\rangle - 2\Omega\langle \overline{\rho\, u_s}\rangle + \left\langle \overline{\hat{e}_\phi \cdot \frac{1}{\mu_0}(\nabla \times B)\times B}\right\rangle \tag{4}$$
$$\equiv F_{\rm R} + F_{\rm C} + F_{\rm L}\,,$$

where $j = (\nabla \times B)/\mu_0$ is the current, the magnetic permeability $\mu_0 = 4\pi \times 10^{-7}$ in SI units, and $\hat{e}_z$ is the unit vector in the azimuthal direction. Here $\bar{f}$ and $\langle f\rangle$ denote the ϕ-average (i.e., the axisymmetric part) and the z-average from z_+ to z_-, respectively, for an arbitrary function f. Outside the tangent cylinder, which is an imaginary cylinder circumscribing the inner shell, $z_\pm = \pm\sqrt{r_{\rm o}^2 - s^2} \equiv \pm H$ where $r_{\rm o}$ is the radius of the conducting region: hereafter we only consider the region outside the tangent cylinder. From the divergence theorem, and the continuity equation (1), the Coriolis force $F_{\rm C}$ vanishes, i.e., there is no net mass flux across a given cylindrical surface. When the inertia including the Reynolds term $F_{\rm R}$ (and viscosity) is negligible compared with the Coriolis and Lorentz forces $F_{\rm L}$ (i.e., magnetostrophic balance), the equation yields a steady state, $\int \hat{e}_\phi \cdot (\nabla \times B)\times B/\mu_0\, dS = 0$, termed the Taylor state (Taylor 1963) by which the magnetic field configuration is constrained.

Allowing small perturbations about this state yields waves/oscillations (see the detailed derivation in Teed et al. (2014); Hori et al. (2019)). We split magnetic field and velocity into their temporal mean and fluctuating parts, which are hereafter denoted by tildes and primes, repectively, i.e., $\widetilde{f} = (1/\tau)\int f dt$ and $f' = f - \widetilde{f}$ where τ is a time window of integration and $\widetilde{f'} = 0$. Substituting the induction equation (3) into the Lorentz term $F_{\rm L}$ of (4) and assuming that an ageostrophic term is sufficiently small, we get a single equation:

$$\frac{\partial^2}{\partial t^2}\frac{\langle \overline{u_\phi'}\rangle}{s} - \frac{1}{s^3 h\langle\overline{\rho}\rangle}\frac{\partial}{\partial s}\left(s^3 h\langle\overline{\rho}\rangle U_{\rm A}^2 \frac{\partial}{\partial s}\frac{\langle \overline{u_\phi'}\rangle}{s}\right) = \frac{\partial}{\partial t}\frac{F_{\rm R} + F_{\rm LD}}{s\langle\overline{\rho}\rangle}\,, \tag{5}$$

where $h = z_+ - z_-$ is the height of the cylinder of radius s along the z axis, i.e., $h = 2H$ outside the tangent cylinder. The left hand side of (5) presents the homogeneous part of the PDE and the equation of torsional Alfvén waves. Terms on the right hand side can be interpreted as forcing to the wave equation, where $F_{\rm LD}$ denotes the Lorentz force $F_{\rm L}$ excluding the restoring part for the wave. In the restoring force $U_{\rm A}^2 = \langle \widetilde{\overline{B_s^2}}\rangle/\mu_0\langle\overline{\rho}\rangle$, representing the squared Alfvén speed given by cylindrical averages of radial field B_s. The homogeneous equation describes waves propagating in cylindrical radius s with the speed $U_{\rm A}$. They may travel either inwardly ($-s$) or outwardly ($+s$), and may also superpose to give a standing wave referred to as "oscillations". Their schematic illustration is shown in Fig. 3. Typical timescales can be interannual to decadal in Earth and Jupiter (Sects. 2.2 and 2.4). Classically, these waves are ideally supposed to be non-dispersive; in reality they could be dispersive owing to the geometry and dissipation. The Reynolds forcing $F_{\rm R}$ likely plays a minor role in Earth's fluid core, as there is no exchanges with the rocky mantle and the reduced importance of inertia signified by the small Ro. This implies that
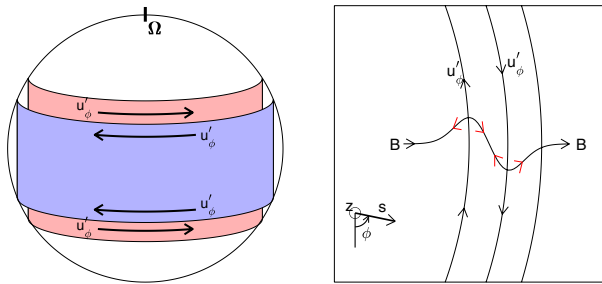
Fig. 3 Schematic illustration of torsional Alfvén waves/oscillations (adapted from Hori et al. (2022))

the Lorentz force F_{LD} is a major driver (Braginsky 1970; Teed et al. 2015). In Jupiter the lack of rigid boundaries and the presence of significant zonal flows in the molecular envelope is likely to make the Reynolds forcing F_R more significant than F_{LD} (Hori et al. 2019).

2.2 Torsional waves in Earth's core

Torsional waves are best illustrated in the geodynamo through both observations and simulations. Early studies (e.g., Braginsky 1970) sought possible wave motion on a ~60 year timescale, which is a relevant peak in the geomagnetic variation as we shall see below. Zatman and Bloxham (1997) extended those investigations to find fluctuations in the azimuthal component of core flows that were inverted from the magnetic secular variation. With the torsional oscillation theory they attempted to infer the 1d structure of the Alfvén speed U_A and to estimate a $\langle \widetilde{B_s^2} \rangle^{1/2}$ of the order 0.1 mT within the dynamo.

Meanwhile, scaling properties of convection-driven dynamos (Sect. 1.2) suggested an internal field strength of the order 1 mT, implying a shorter timescales for torsional oscillations. Gillet et al. (2010) explored signals of several years in core flow models and attributed them, not the decadal signal, to the torsional oscillations. They also evaluated the angular momentum exchange with the rocky mantle to show the fluctuations were compatible with a variation in length-of-day, i.e., the rotation rate of the planet, in which a period ~6 years was seen.

Their picture raised further interesting questions. First, the identified wave exhibited outward propagation toward the equator from deep and appeared to be excited quasi-periodically; when it approached the equator, no clear reflections at the equator were observed. Indeed numerical dynamo simulations embraced travelling waves, rather than standing ones (e.g., Wicht and Christensen 2010; Teed et al. 2014; Schaeffer et al. 2017). Schaeffer and Jault (2016) pointed out that the dissipation across the core-mantle-boundary would inhibit wave reflections there, to leave travelling modes only: the processes were nicely demonstrated by the solution of an initial value problem (Gillet et al. 2017). In contrast, spherical magnetic convection simulations with no couplings with the mantle being assumed reproduced the

one-way propagation excited near the tangent cylinder repeatedly (Teed et al. 2019): Fig. 4 depicts such a case. This dynamics is likely a natural consequence of the convection in the fluid core, which is most vigorous near the tangent cylinder in which buoyancy sources arise from the inner core solidification. The simulation by Teed et al. (2019) reveals that it is possible to launch an axisymmetric disturbance of the Alfvén frequency there, which is absorbed as it approaches the rigid boundary of the rocky mantle.

However observationally, whilst core flow inversions illustrate the wave-like patterns, these signals do not appear in the magnetic data clearly. Silva et al. (2012) examined over decadal timeseries of the geomagnetic secular acceleration, $\partial^2 B_r / \partial t^2$, at chosen locations in terms of the Fourier transform and empirical mode decomposition and reported identification of ~6 year periodicities. We shall address this in the following subsection.

2.3 Geomagnetic data revisited

We here revisit the geomagnetic data for torsional waves, given the recent improvement in observational datasets. Moreover, data-driven techniques are drastically advancing and are now capable of extracting signals more efficiently. Here we adopt a technique called dynamic mode decomposition, DMD (e.g, Schmid 2010; Kutz et al. 2016). This may be regarded as an update of the Fourier transform and proper orthogonal decomposition (POD) — equivalent to the principal component analysis (PCA) — and may approximate spatio-temporal data in the form of the sum of normal modes. For instance, a given dataset $X = X(\theta, t)$ may be approximately represented as $\sum_{j=1}^{r} b_j \Phi_j(\theta) \exp(\lambda_j t)$ where b_j is real and λ_j and Φ_j are complex. Here $\mathrm{Im}\lambda_j$, $\mathrm{Re}\lambda_j$, b_j, and $\Phi_j(\theta)$ denote, respectively, the frequency, growth rate, magnitude, and spatial structure of the j-th DMD mode (out of the total r modes). The outcomes can therefore be compared with normal mode solutions of the wave equation (5) [see
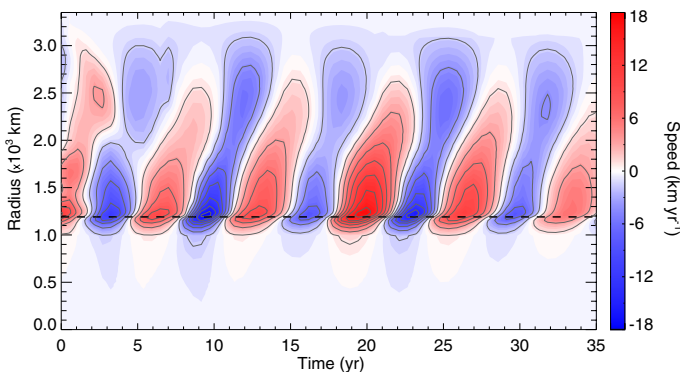

Fig. 4 Torsional Alfvén waves seen in a spherical convection simulation for Earth's core (adapted from Teed et al. (2019)). The zonal velocity fluctuation $\langle u'_\phi \rangle$ is shown in time-cylindrical radius domain

Appendix A and Figure A1a for normal mode calculations]. The methodology was utilised in spherical MHD simulations (Hori et al. 2020b).

The data to be analysed is the axisymmetric fluctuating part of both the cylindrically-radial secular variation $\partial \overline{B}_s / \partial t$ and the azimuthal core flow $\overline{u'_\phi}$ on the core surface r_{core} between 1940–2005: the datasets depends on latitude θ and time t. These are computed from ensemble averages of 50 realisations given by the up-to-date assimilation model (Gillet et al. 2019) that we refer to as cov-obs2019 hereafter. The model gives the coefficients of spherical harmonics of the magnetic potential, termed the Gauss coefficients, and the equivalent values for the core flow. So we first calculate the component $\partial B_s / \partial t$ and u_ϕ at r_{core}, with the Schmidt normalised associated Legendre function. We then compute their axisymmetric parts, average over the realisations, and remove the temporal means at each θ. To seek wave signals that have the form $[\overline{B'_s}, \overline{u'_\phi}] \propto \exp i\omega t$, we put the two sets of the latitude-time data together into the decomposition analysis and perform the DMD over the dataset. Here we examine the data at 140 gridpoints between $\pm 69.5°$ and for 65 snapshots sampled every year. We then introduce a delay coordinate to stack the data and to capture either travelling or standing waveforms (e.g., Kutz et al. 2016): the methodology is also described in Hori et al. (2022). As the rms error between the input and reconstructed datasets are found to be minimised for a delay coordinate of 2, we set this parameter below.

Figures 5a and b show the spectrum and the dispersion of the DMD signals, respectively. They show spectral peaks at low frequencies (corresponding to periods of 64.9, 32.3, and 20.9 years) and also local peaks around a period of ∼6 years (the shaded region). The latter comprises of four individual modes (highlighted by coloured symbols), out of which two are found to be low quality ($\text{Im}\lambda / 2\text{Re}\lambda < 4$) — in this case meaning highly dissipative — and two to be high quality ($\text{Im}\lambda / 2\text{Re}\lambda \sim 13$). The two wave-like modes have periods of 6.6 and 6.3 years: we refer to them as Modes 1 and 2, respectively, and highlight them in red and blue. Their latitudinal structures with respect to s are given in figure c: Mode 1 in red has one zero crossing at $s/r_{core} \sim 0.65$. This could be a signature of the first eigenmode of torsional wave (5) [see figure A1a for a background $\widetilde{\overline{B}_s}$ of maximum 3.9 mT]. If this field structure is assumed, the second eigenmode could be predicted: whose frequency is indicated by a vertical line labelled as T_2 in the figures a and b: we refer to the chosen mode as Mode 3 (in cyan). The three Modes are reconstructed for the spatio-temporal structure of $\overline{u'_\phi}$ in figures d–e. The pattern shows the travelling nature in either hemisphere nicely, suggesting the DMD analysis reproduces the early reports (e.g., Gillet et al. 2010) and extracts the relevant modes.

The corresponding pattern in the magnetic field $\partial \overline{B}_s / \partial t$ is now visualised in figures f–g. We can detect some travelling features; however the detected signal only exhibits a magnitude of 1% or smaller of the overall variation. This in part explains why the torsional waves are not easily detected in magnetic data. Meanwhile the analysis here demonstrates how the data analysis is capable of pulling out such a tiny, but physically important, signal.
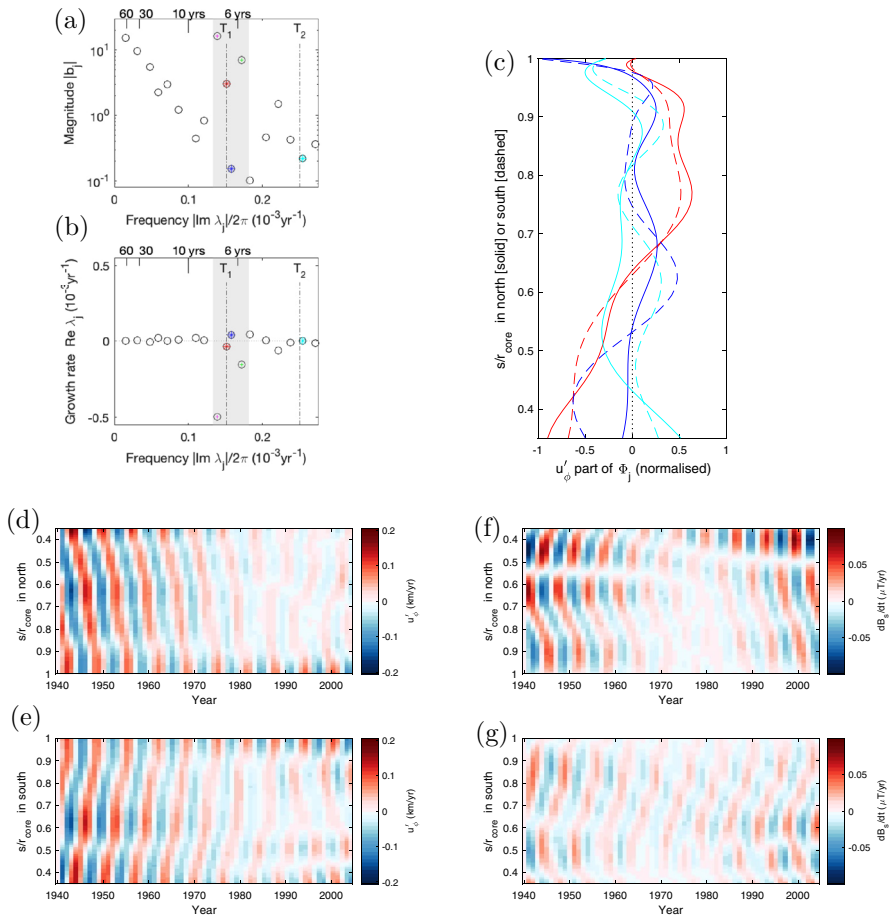
Fig. 5 DMD analysis of axisymmetric geomagnetic secular variation and core flow in 1940–2005 (produced from Gillet et al. (2019)). **a** Spectral and **b** dispersion diagrams of the dataset comprising of $\overline{u'_\phi}(\theta, t)$ and $\partial \overline{B_s}/\partial t(\theta, t)$. Periods are represented in years on the top of each panel. Symbols highlighted in color indicate Modes in a window of period $5.5 - 7.5$ years (shaded region). Individual Modes in the window are highlighted by different colors and symbols: we refer to the red and blue asterisks as Modes 1 and 2, respectively, whilst the magenta and green crosses represent dissipative modes. The vertical dashed-dotted line labelled by T_i indicates the frequency of the i-th TW normal mode for a background field $\langle \overline{B_s^2} \rangle^{1/2} \lesssim 3.9$ mT (see figure A1a). One Mode found in the vicinity of the T_2 line is also indicated in cyan and is referred to as Mode 3. **c** Latitudinal structures of $\overline{u'_\phi}$ for Modes 1 (red), 2 (blue), and 3 (cyan) are represented with respect to s/r_{core}. Solid (dashed) curves show its profile in the northern (southern) hemisphere. **d–e** Reconstructed spatiotemporal structure of $\overline{u'_\phi}$ for the superposition of Modes 1–3. **f–g** Similar to figures d–e but of $\partial \overline{B_s}/\partial t$. In **d,f** northern and **e, g** southern hemispheres

2.4 Torsional oscillations in Jupiter

Given the presence of torsional waves in Earth's fluid core, one might expect to find them in other planets. Indeed the potential for their discovery has been growing as planetary exploration and numerical modelling advance. Modern numerical
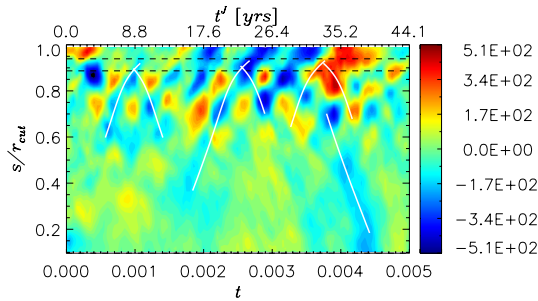
Fig. 6 Similar to Fig. 4 but in a dynamo simulation for Jupiter's metallic hydrogen region (adapted from Hori et al. (2019)). Here the cylindrical radius s is normalised by the cutoff radius, $r_{cut} \sim 0.96R_J$, of the simulation. White curves indicate phase paths of the Alfvén speed U_A. A dimensional time is represented in years on the top of the panel. Horizontal dashed lines indicate radii across which density and electrical conductivity drop by orders

dynamos, that implement the transition from the metallic to molecular hydrogen envelopes of Jupiter, have succeeded in reproducing the dipole-dominated, global magnetic field (Jones 2014; Gastine et al. 2014b). Using those numerical models Hori et al. (2019) proposed that torsional Alfvén waves on timescale of the order 1–10 years could be excited in the gas giant too; zonal fluctuations seen for a fiducial case are exhibited in Fig. 6. Moreover the simulations demonstrated that Jovian torsional waves could be standing waves; here waves would partially reflect from the interface that is created by the abrupt change in the electrical conductivity as the metallic hydrogen transits to the molecular hydrogen. The ratio of reflection and transmission is essentially determined by the wavenumber of the oscillation and the skin depth for the mode.

Such fluctuations in zonal velocity could impact on the dynamics beyond the metallic region. One consequence could be fluctuations in length of day — as happens in Earth. The simulations above suggested a magnitude of the order 10^{-2} s or smaller, so likely very tiny. Nonetheless it is worth noticing that the planet's rotation rate, or the System III coordinate system determined from its periodic radio emission, is measured to such precision and its variation was the subject of some debate (e.g., Higgins et al. 1996). Another consequence is remarkable in a gaseous planet: zonal flow fluctuations arising from MHD waves may partly transmit into the overlying poorly-conducting envelope, whilst dissipating. This implies the deep oscillation might be probed through near-surface observations, such as visible, infrared, and microwave measurements. Now the Juno's multiple measurements were reported to be consistent with the surface zonal wind extending down to thousands of kilometres, 0.93–0.96R_J (e.g., Kaspi et al. 2018; Moore et al. 2019).

Interestingly, ground-based telescope observations have witnessed intradecadal to decadal variations of the surface (e.g., Fletcher 2017). To seek the tropospheric dynamics, Antuñano et al. (2019) investigated infrared images taken at ~5 μm wavelength for more than 30 years and found cycles of 4–9 years in latitudinal bands between ~40°N and ~40°S. Those observations might be accounted for by the torsional oscillations arising from the interior (Hori et al. 2022). The scenario
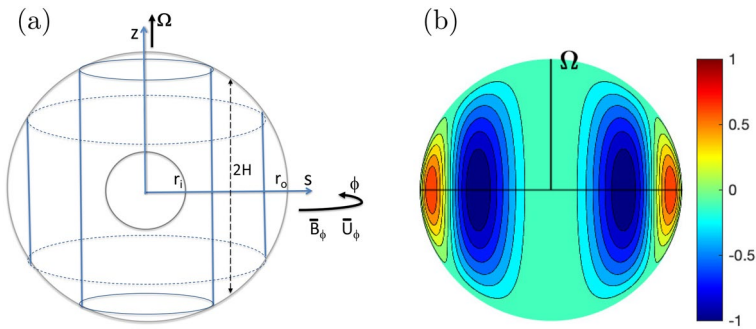
Fig. 7 a The 2d quasi-geostrophic model adopted. **b** An eigenfunction for background $\widetilde{B_\phi} \propto s$ and constant ρ (Malkus 1967). Normalised radial velocity u_r is presented in the meridional plane with respect to the rotation axis $\mathbf{\Omega}$

necessitates the processes coupling amongst the modulations in zonal flows, the tropospheric convection, and its infrared observation. This exemplifies the notable dynamics of a gaseous planet in contrast with a terrestrial planet.

3 Magnetic Rossby waves

Now we move onto nonaxisymmetric modes. They can be classified into three categories: Rossby waves, Alfvén waves, and waves that have certain characteristics of both, termed magnetic Rossby waves. First we discuss their fundamental properties via linear theory (Sect. 3.1) and explore their relevance in the geodynamo and the geomagnetic westward drift (Sect. 3.2); then we move on to discuss weakly nonlinear effects (Sect. 3.3).

3.1 Fundamentals

Guided by the literature (e.g., Hide 1966; Hori et al. 2018), we describe these nonaxisymmetric waves for anelastic fluids. We here adopt an illustrative quasi-geostrophic model for rotating spherical shells (e.g., Busse 1970, 1976; Canet et al. 2014): the 2d model is schematically illustrated in Fig. 7a. This approach ought to be distinguished from the full problem (1)–(3), as pioneered by Malkus (1967). One of his solutions is exhibited in Fig. 7b, representing a symmetric mode with respect to the equator, i.e., a magnetic Rossby mode.

Our basic equation here is the vorticity equation. We take the curl of the momentum equation (2) in cylindrical coordinates to yield the equation for the axial (z) component of vorticity, $\boldsymbol{\xi} = \nabla \times \boldsymbol{v}$. This ensures conservation of the potential vorticity $(2\Omega + \xi_z)/\overline{\rho}H$ in the absence of terms other than the inertial and Coriolis forces.

The classic Rossby waves arise from vortex tube stretching and shrinking to conserve the potential vorticity.

To seek the MHD equivalent we consider the z-component of the vorticity equation averaged over z,

$$\frac{\partial}{\partial t}\langle\overline{\rho}\xi_z\rangle + \langle\nabla_{\mathrm{H}}\cdot\overline{\rho}(\boldsymbol{u}\xi_z - \boldsymbol{\xi}u_z)\rangle - 2\Omega\left\langle\frac{\partial}{\partial z}\overline{\rho}u_z + u_s\frac{\partial\overline{\rho}}{\partial s}\right\rangle = \langle\nabla_{\mathrm{H}}\cdot(\boldsymbol{B}J_z - J B_z)\rangle \quad (6)$$

where $\nabla_{\mathrm{H}}\cdot\boldsymbol{A} = (1/s)\partial(sA_s)/\partial s + (1/s)\partial A_\phi/\partial\phi$ for a vector $\boldsymbol{A}$. We separate the variables, $\boldsymbol{u}$ and $\boldsymbol{B}$, into the temporal mean (denoted by tildes) and fluctuation (by primes) in time. Linearising (6), together with (3), yields

$$\frac{D^2\langle\xi_z'\rangle}{Dt^2} + \beta\frac{D\langle u_s'\rangle}{Dt} = \frac{1}{\mu_0\langle\overline{\rho}\rangle}\left\langle(\widetilde{\boldsymbol{B}}\cdot\nabla_{\mathrm{H}})(\widetilde{\boldsymbol{B}}\cdot\nabla_{\mathrm{H}})\xi_z'\right\rangle, \quad (7)$$

provided $\partial\langle\overline{\rho}\xi_z\rangle/\partial t \sim \langle\overline{\rho}\rangle\partial\langle\xi_z'\rangle/\partial t$. Now the Coriolis term is represented via the beta parameter. For the incompressible/Boussinesq fluids this is given by the topographic effect,

$$\beta = -\frac{2\Omega}{H}\frac{dH}{ds}, \quad (8)$$

as non-penetrative conditions at the boundaries imply $u_z = \pm u_s\,dH/ds = \mp u_s\,s/H$ at $z = \pm H$ outside the tangent cylinder (e.g., Busse 1970). When the density varies significantly, the beta effect instead arises from compressible effects,

$$\beta = -\frac{2\Omega}{\langle\overline{\rho}\rangle}\frac{d\langle\overline{\rho}\rangle}{ds}, \quad (9)$$

where the z-integral of the third term of (6) is performed (e.g., Gastine et al. 2014a; Sasaki et al. 2018). Here note the validity of this expression depends on the dynamics of the anelastic fluid, particularly on the z-integral of the Coriolis term, i.e., to what extent the vorticity is stretched along z between the boundaries $\pm H$. For more discussions on compressible beta effects we refer to Glatzmaier et al. (2009); Jones et al. (2009); Verhoeven and Stellmach (2014); and Busse and Simitev (2014). In Earth's fluid core in which the density change is minor and there are solid boundaries, the topographic effect is clearly a reasonable driver. However, the compressible effect will be relevant in Jupiter's interior.

Introducing the streamfunction ψ for the velocity perturbation, e.g., $\langle\boldsymbol{u}'\rangle \sim \nabla_{\mathrm{H}}\times\psi(s,\phi,t)\hat{\boldsymbol{e}}_z$ with $\hat{\boldsymbol{e}}_z$ being the unit vector in the direction of the rotation axis, we find (7) to give a wave equation. We now suppose that the background magnetic field and flow are both steady and axisymmetric to seek solutions of the form of $\psi = \hat{\psi}\exp\mathrm{i}(m\phi - \omega t)$. Here the background flow is supposed to be dominated by the zonal component. The wave equation then becomes

$$\frac{1}{\mu_0\langle\overline{\rho}\rangle}\left\langle\overline{\widetilde{B}_s}\frac{d}{ds}\overline{\widetilde{B}_s}\frac{d}{ds}\left(\frac{1}{s}\frac{d}{ds}s\frac{d}{ds} - \frac{m^2}{s^2}\right)\hat{\psi}\right\rangle + (\hat{\omega}^2 - \omega_{\mathrm{M}}^2)\left(\frac{1}{s}\frac{d}{ds}s\frac{d}{ds} - \frac{m^2}{s^2}\right)\hat{\psi} + \frac{\beta\hat{\omega}m}{s}\hat{\psi} = 0,$$
$$(10)$$

where $\hat{\omega} = \omega - \langle \widetilde{\overline{U_\phi}} \rangle m/s$, and the squared Alfvén frequency is given by $\omega_M^2 = \langle \widetilde{\overline{B_\phi^2}} \rangle m^2 / \mu_0 \langle \overline{\rho} \rangle s^2$. This equation goes singular when $\sqrt{\widetilde{\overline{B_s^2}} / \mu_0 \langle \overline{\rho} \rangle}$, the local speed of torsional Alfvén waves, crosses zero. If the torsional wave is slow compared with the Alfvén and Rossby waves travelling in azimuth, eq. (10) may be further reduced to a second-order ODE:

$$(\hat{\omega}^2 - \omega_M^2)\left(\frac{1}{s}\frac{d}{ds}s\frac{d}{ds} - \frac{m^2}{s^2} \right)\hat{\psi} + \frac{\beta\hat{\omega}m}{s}\hat{\psi} = 0 \ . \tag{11}$$

Here a critical layer will appear if $\hat{\omega}^2 \to \omega_M^2$. If this does not occur in the domain, (11) yields a set of two solutions. This eigenvalue problem for different profiles of ω_M^2 in Boussinesq fluids was explored by Canet et al. (2014).

To examine the basic properties of the equation, we here suppose a WKBJ-type solution, $\hat{\psi} = A_0 s^{-1/2} \exp i \int n(s)ds$ [see Appendix B for details], where the local dispersion relation is given by

$$\hat{\omega}^2 - \hat{\omega}\,\omega_R - \omega_M^2 = 0 \ , \tag{12}$$

and the Rossby wave frequency $\omega_R = \beta ms/(m^2 + n^2 s^2 + 1/2)$. The quadratic equation (12) has roots

$$\omega_\pm = \omega_R\left[\frac{1}{2} \pm \frac{1}{2}\sqrt{1 + 4\frac{\omega_M^2}{\omega_R^2}} \right] \ . \tag{13}$$

In the limit $\omega_M^2/\omega_R^2 \gg 1$, e.g., high wavenumbers for a given basic state, these simply yield the Alfvén waves along the toroidal field. Their unique properties become evident in another limit $\omega_M^2/\omega_R^2 \ll 1$ to yield

$$\omega_+ \sim \omega_R\left(1 + \frac{\omega_M^2}{\omega_R^2} \right) \quad \text{and} \quad \omega_- \sim -\frac{\omega_M^2}{\omega_R} \ . \tag{14}$$

The fast modes, with frequency ω_+, are essentially equivalent to the hydrodynamic waves. Their timescales are basically ruled by β, or the planet's rotation rate, but are shorter in the presence of the background magnetic field. Their phase velocity is prograde in a thick shell problem (such as that applicable for the Earth's fluid core) (Busse 1970, 1986), while the group velocity is retrograde. Note that these directions appear to be opposite from the conventional Rossby waves in the atmosphere. Fig. 8 demonstrates a fast wave seen in Jovian dynamo simulations, in which the compressible beta effect plays a role.

The slow modes, with frequency ω_-, are unique to the rotating MHD system, travelling retrogradely; the frequency is given by the ratio of the squared Alfvén frequency to the Rossby frequency. Hence they are sensitive to $\langle \widetilde{\overline{B_\phi^2}} \rangle$, or the toroidal field strength. Their timescales may vary from 10^1 to 10^4 years in Earth's fluid core, indicating a link to the centennial geomagnetic westward drift (Hide 1966)
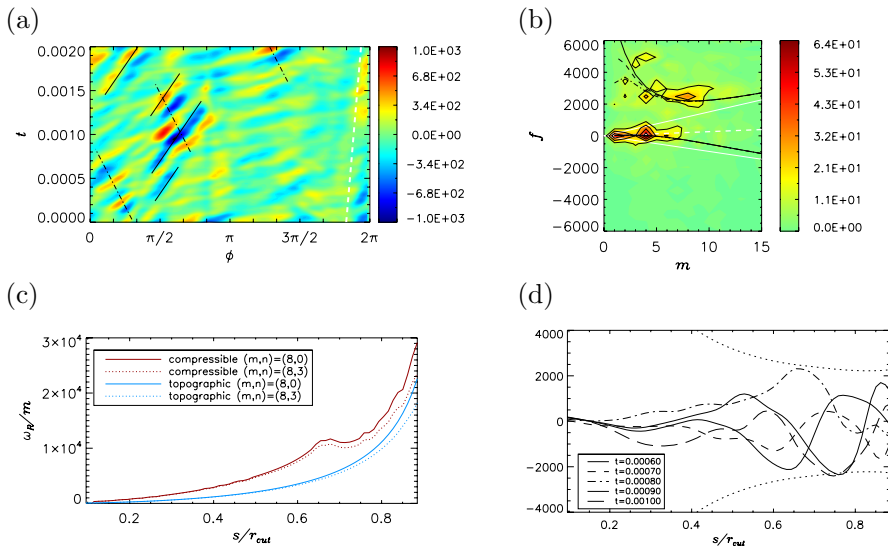
Fig. 8 Fast magnetic Rossby waves seen in a jovian dynamo simulation (run E in Jones (2014) and Hori et al. (2019)). **a** Azimuth time section and **b** wavenumber-frequency power spectrum of $\langle u'_s \rangle$ at $s = 0.25r_{cut} \sim 0.24R_J$. In figure a, solid black lines represent phase paths of fast compressible Rossby waves plus the zonal flow advection, $\omega_+/m + \langle \overline{U_\phi} \rangle/s$, for $m = 8$ and $n = 0$: dashed-dotted lines indicate their group velocity, $\partial\omega_+/\partial m + \langle \overline{U_\phi} \rangle/s$. In figure b, black curves show the expected dispersion relations of advection plus wave ω_+ for the compressible beta parameter and $n = 0$ (solid), 3 (dashed), and 5 (dashed-dotted). White dashed lines for the advection only; white solid curves for the advection plus the Alfvén wave ($\pm\omega_M$). **c** Phase speeds of compressible (red) and topographic (blue) Rossby waves, ω_R/m, as a function of normalised s. (d) Radial profiles of $\langle u'_s \rangle$ at $\phi \sim 2\pi/3$. Curves exhibit snapshots at different times, which are indicated in the legend. Dotted ones indicate the expected variability $s^{-3/2}$ [see Appendix B for details]

(Sect. 3.2). The dispersive nature of this mode is also noticeable. For the case of topographic effects, the slow mode dispersion relation (14) may be rewritten as

$$\omega_- \sim -\frac{\langle \overline{B_\phi^2} \rangle(r_o^2 - s^2)}{2\mu_0\langle\overline{\rho}\rangle\Omega s^4}m(m^2 + s^2n^2) \,, \tag{15}$$

where the geometrical effect in the Rossby frequency is omitted. This is reduced to a relationship proportional to m^3 when the azimuthal wavenumber dominates over the radial one. The wave motion is highly dispersive in the ϕ direction; this dispersive nature gives a strong steer to possible nonlinear behaviour (i.e., the presence of solitons as discussed in Sect. 3.3). This is not the case when the radial structure is more complicated, i.e., $m^2 \ll s^2n^2$; in that case the ϕ-propagation is largely non-dispersive while the s-propagation is weakly dispersive. We here recall that both magnetic Rossby modes are capable of travelling in s: this is analogous to the atmospheric version which may travel in latitude too (e.g., Vallis 2017).
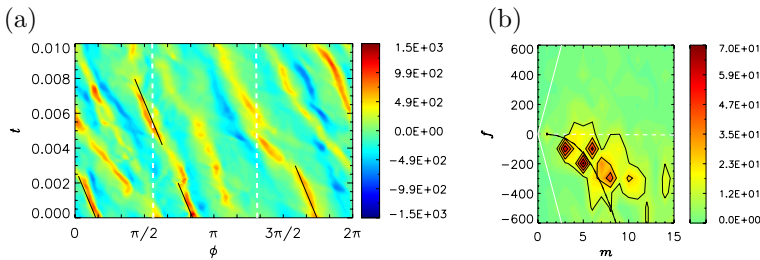
Fig. 9 Slow magnetic Rossby waves in a geodynamo simulation (adapted from Hori et al. (2018)). **a** Azimuth time section and **b** wavenumber-frequency power spectrum of $\langle u_s' \rangle$ at the mid radius $s = 0.5 r_{core}$. In figure a solid black lines represent phase paths of slow magnetic Rossby waves plus the zonal flow advection, i.e., $\omega_-/m + \langle \overline{\overline{U_\phi}} \rangle /s$ for $m = 5$ and $n = 0$; white dashed lines indicate the advection speed only. In figure b, solid black (white) curves represent the expected dispersion relations of advection plus the wave $\omega_\pm$ (ω_M) for the topographic beta parameter $n = 0$. White dashed lines for the advection only

All theory needs to be re-addressed when $\left\| \overline{\overline{\widetilde{B}_s}} \partial / \partial s \right\| \gg \left\| (\overline{\overline{\widetilde{B}_\phi}}/s) \partial / \partial \phi \right\|$. As indicated from (7) or (10) the slow mode for the case would imply highly dispersive motion in s. This seems to be the regime recently explored by Gerick et al. (2021), who computed eigenmodes in an extended 2d model for a nonaxisymmetric background $\widetilde{B}_s$ to obtain high wavenumber modes for the interannual westward drift (Sect. 3.2).

3.2 Magnetic Rossby waves in the Earth

Slow magnetic Rossby waves were proposed by Hide (1966) to explain the ~300 year geomagnetic westward drift (Sect. 1). This migration has been seen in centennial models (e.g., Finlay and Jackson 2003) and in millennial models (e.g., Hellio and Gillet 2018; Nilsson et al. 2020). A complementary scenario to this is that the westward drift arises because of the advection by large-scale flows in the geodynamo (e.g., Bullard et al. 1950; Aubert et al. 2013). It is more likely that the observed feature consists of a combination of advection and wave propagation; some early works on numerical dynamos pointed out that migration speeds seen in simulations did not match the flow advection speed (Kono and Roberts 2002; Christensen and Olson 2003).

Using updated geodynamo simulations, Hori et al. (2015) re-addressed nonaxisymmetric motions in terms of the 2d theory above, and demonstrated that the retrograde drifts in the simulations were well explained by slow waves (15) riding on the mean flow advection $\langle \overline{\overline{U_\phi}} \rangle m/s$ (Fig. 9). The nonaxisymmetric waves may be excited through any driving mechanism; here convection in the spherical shell plays a major role. The preferred wavenumber, or the frequency, is thus determined by convective activities. The nature of the observed waves clearly depends on the regime of the driving mechanism: in the case of convection a slow wave will be favourable when the magnetic diffusion time is longer than the thermal one, while the opposite
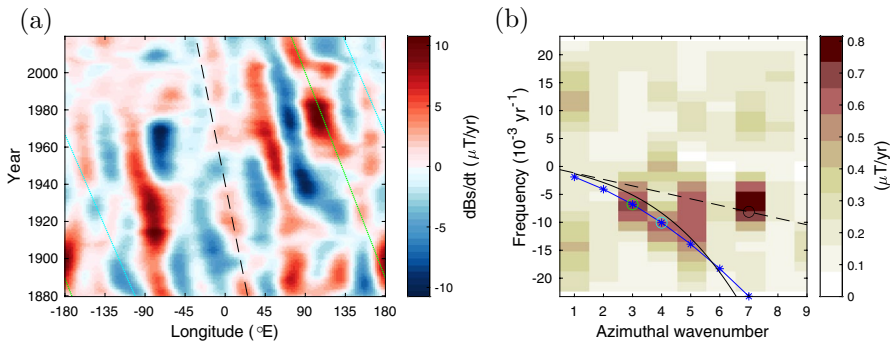
Fig. 10 Nonaxisymmetric motion of geomagnetic secular variation, $\partial B_s/\partial t$, in 1880–2015 (produced from Gillet et al. (2019)). **a** Longitude-time section, Hövmoller diagrams, and **b** 2d spectrum, the sum over 39–41°N. In figure a the green, cyan, black lines indicate the speeds of signals at $m = 3$, 4, and 7, respectively, as identified by circles in the spectrum. In figure b the dashed line represents $f_{adv} = U_0 m/2\pi s$ given $U_0 = 0.32°/\text{yr}$ at the radius $s = 0.77 r_{core}$ (Pais et al. 2015; Hori et al. 2015); the black solid curve represents $f = f_{adv} + \omega_-/2\pi$, based on the local theory (15) for $\langle \widetilde{B_\phi^2} \rangle^{1/2} = 15$ mT; blue asterisks indicate $f = f_{adv}$ plus the frequency of the first normal mode solutions (11) for Malkus field $\langle \widetilde{B_\phi} \rangle \propto s$ of magnitude 13mT (see figure A1b)

regime will yield other modes including diffusive modes travelling progradely (Busse 1976; Finlay 2008; Hori et al. 2014). Analyses of the simulations confirmed that the slow waves emerged when the magnetostrophic terms were dominant in the vorticity equation (6) (Hori et al. 2018). The identification of those waves, as well as torsional Alfvén waves, may signify a dynamo in the magnetostrophic regime.

It is useful to examine the geomagnetic data for nonaxisymmetric components. Figure 10a displays the longitude-time section, from 1880 to 2015, of the secular variation, $\partial B_s/\partial t$, at latitude ~40°N corresponding to $s/r_{core} \sim 0.77$, in cov-obs2019. The westward drift, clearly visible on this timescale, appears to consist of multiple drift speeds. This is evident by the 2d FFT spectrum in figure b. Here a linear relation, $\omega \propto m$, indicated by the dashed line, represents an advection effect by mean flow. Clearly this simple advection model can not explain the multiple signals observed. We add the dispersion relations of the slow wave too: the black solid curve for the local theory (15) for $\langle \widetilde{B_\phi} \rangle^{1/2} \sim 15$ mT and blue asterisks for normal mode solutions provided a background $\widetilde{B_\phi} \propto s$ of maximum 13 mT (Appendix A and Figure A1b). Those speeds for chosen m are indicated by different lines in the figure a. This attempt is inconclusive but indicative that today's geomagnetic datasets are capable of capturing the signatures of waves. It would be crucial to analyse them on multiple timescales; the slow wave timescale may vary by a few orders of magnitude (see above). Probing the slow wave will enable the estimation of the toroidal magnetic field (Hori et al. 2015), which is confined within the dynamo region, i.e., inaccessible through direct measurements.

Beyond the framework above, a zoo of nonaxisymmetric waves is being explored. State-of-the-art numerical geodynamo calculations exhibit different wave classes (e.g., Aubert and Finlay 2019; Aubert and Gillet 2021) such as Alfvén modes about

inhomogeneous poloidal part $\widetilde{B}_s$ and also fast Rossby modes likely. These have been linked geomagnetic jerks (Sect. 1) and to nonlinear interactions with the convective dynamics for the dynamo. More recently, based on the linear calculations by Gerick et al. (2021), Gillet et al. (2022) attributed slow modes of high radial wavenumber for a background $\widetilde{B}_s$ to the equatorial westward drift of ~6 years (Sect. 1.3). An alternative idea for the rapid drift is that Rossby waves are excited in the stratified layer at the top of the core, as an MAC wave (Buffett and Matsui 2019). These are ongoing topics; we shall remark further in the final section.

3.3 Finite amplitude effects

A novel finding by the numerical simulations described above was the sharp waveform of the slow wave (e.g., Fig. 9a). These are isolated and steepened, rather than forming wave trains as expected for a linear dispersive wave. Moreover, their crests appear to be cleaner than the troughs. Those observations are reminiscent of cnoidal waves and solitons of finite amplitude, which are both known to be solutions of the Korteweg-de Vries (KdV) equation. Indeed, the approximated dispersion relation (15) has the dispersive term proportional to m^3, as in the KdV equation. Weakly nonlinear analyses were recently explored (Hori 2019; Hori et al. 2020a) in terms of 2d annulus models (Busse 1976) and spherical models (Canet et al. 2014). This contrasts with analyses in equatorial shallow-water MHD (London 2017), in which fast modes in a stratified environment were a primary focus. (Hydrodynamic Rossby waves are known to shape coherent structures and to be governed by soliton equations in certain regimes (e.g., Redekopp 1977; Williams and Yamagata 1984); those solutions were proposed as an explanation for the Jupiter's Great Red Spot.)

The model setting adopted by Hori (2019) and Hori et al. (2020a) is essentially same as above (Fig. 7a). For simplicity the magnetic field is also assumed to be two dimensional so that it can be represented by the magnetic potential g such that $\boldsymbol{B} = \nabla \times g(s, \phi, t)\hat{\boldsymbol{e}}_z$; this is analogous to the streamfunction ψ for the velocity, $\boldsymbol{u} = \nabla \times \psi(s, \phi, t)\hat{\boldsymbol{e}}_z$. Also we suppose the density is constant and the beta parameter is topographic. Following a standard multiple-scale technique called the reductive perturbation method, we introduce slow variables with small perturbation ϵ ($\ll 1$) such that $\tau = \epsilon^{3/2}t$ and $\zeta = \epsilon^{1/2}(\phi - ct)$ and expand the two variables to get asymptotic solutions such that $[\psi, g] = [\psi_0, g_0] + \epsilon[\psi_1, g_1] + ...$ Hence a long-wave limit is being studied.

The zeroth order is given by the basic state. At the first order $\mathcal{O}(\epsilon)$ the two governing equations yield a linear, 2nd-order homogeneous PDE for g_1. Assuming a separable solution in form $g_1 = \Phi(s)G(\zeta, \tau)$ reduces the problem to an ODE in dimensionless form,

$$\mathcal{L}\Phi \equiv \left\{ \frac{\overline{\overline{B_\phi}}}{\beta s}\left[\frac{\overline{\overline{B_\phi}}}{s}\frac{d}{ds}s\frac{d}{ds} - \frac{d}{ds}\frac{1}{s}\frac{d}{ds}s\overline{\overline{B_\phi}} \right] + \left(\frac{\overline{\overline{U_\phi}}}{s} - c \right) \right\}\Phi = 0 \,, \qquad (16)$$
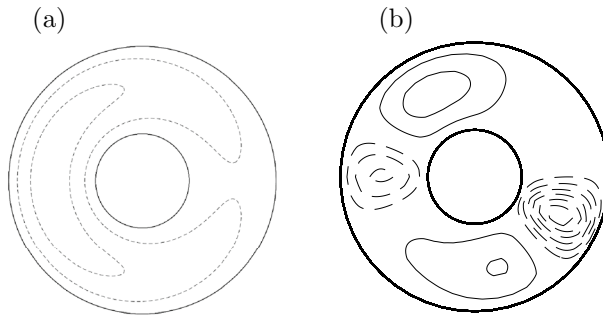
Fig. 11 **a** 1-soliton and **b** N-soliton solutions of slow magnetic Rossby waves for Malkus field, $\overline{\overline{B_\phi}} = s$ (after Hori et al. (2020a)). Streamfunction ψ in the equatorial plane in snapshots. Dashed (solid) curves indicate their negative (positive) values, implying anticyclonic (cyclonic) motion

where $\mathcal{L}$ denotes the linear differential operator comprising of s, d/ds, $\overline{\overline{B_\phi}}$, β, $\widetilde{\overline{U_\phi}}$, and c. This is an eigenvalue problem with eigenvalues c and associated eigenfunctions Φ, together with appropriate boundary conditions. Here it is worth noting that the equation becomes singular as $\overline{\overline{B_\phi}}^2/\beta \to 0$ but this is unlikely as $\widetilde{\overline{U_\phi}}/s \to c$. This is distinct from the hydrodynamic cases; there Redekopp (1977) addressed solitary Rossby waves in the vicinity of the critical layer when a wave speed approaches the mean flow speed. What happens around any magnetic critical layer, including its continuous solutions, is entirely uncertain.

Focusing on the discontinuous solutions, we proceed to the next order to determine the structural function $G(\zeta, \tau)$. After some algebra, the vorticity and induction equations at $\mathcal{O}(\epsilon^2)$ are found to yield an inhomogeneous PDE for g_2, whose homogeneous part is given as $\mathcal{L}g_2 = 0$. We thus require a solvability condition to suppress the secular terms, yielding

$$\frac{\partial G}{\partial \tau} + \alpha \, G \frac{\partial G}{\partial \zeta} + \gamma \, \frac{\partial^3 G}{\partial \zeta^3} = 0 \, . \tag{17}$$

Here α and γ are determined from the $\mathcal{O}(\epsilon)$-eigenfunction Φ, its adjoint solution $\Phi^\dagger$, and the basic state $\overline{\overline{B_\phi}}$, $\widetilde{\overline{U_\phi}}$, and β: see detailed expressions in Hori et al. (2020a). This evolution of the structural function $G(\zeta, \tau)$, and hence g_1, is therefore governed by the the Korteweg-de Vries equation if the coefficients are both nonzero. Equivalent analyses in the cartesian model (Hori 2019) show that the coefficient of nonlinear effect would be nonzero unless $\overline{\overline{B_\phi}}$, β, and $\widetilde{\overline{U_\phi}}$ are all uniform. This could be readily satisfied for a spherical system, for which β is nonuniform.

In spherical shells Hori et al. (2020a) solved the eigenvalues problem (16) to calculate the coefficients of (17) for different sets of the basic state magnetic fields $\overline{\overline{B_\phi}}$ and velocity profiles $\widetilde{\overline{U_\phi}}$. They found nonzero values for the coefficients for the all cases they explored, implying that the KdV equation is the correct canonical description. As its solutions are well known, our asymptotic solution may be simply

illustrated. Cases for the 1- and N-soliton solutions are demonstrated in Fig. 11. The solitary wave solution as seen in Fig. 11a implies an anticyclonic isolated vortex that is drifting retrogradely with the speed of the linear wave, the order of 10^2 to 10^4 years in Earth's core. Here recall that core flow inversions have revealed an anticyclonic gyre persisting in the fluid core for more than 100 yrs (Fig. 2). An up-to-date geomagnetic model for the past 9000 years was recently reported to exhibit a westward-drifting eastern-western hemispherical asymmetry, with quasi-periodic behaviours of ~1300 years, potentially related to a similar planetary gyre (Nilsson et al. 2022). The origin of the asymmetry has been discussed in terms of couplings with the rocky mantle and the solid inner core (e.g., Aubert et al. 2013). Meanwhile, geodynamo simulations demonstrated the emergence of such a coherent structure as a natural consequence of the fluid dynamics therein (Schaeffer et al. 2017). The soliton solutions above show that the gyre shape can simply be explained using natural nonlinear wave dynamics.

4 Concluding remarks and perspectives

In this paper we have discussed the topic of rotating MHD waves, or MC waves, largely motivated by recent advances of geophysical observation and numerical modelling. The subject embraces rich physics in addition to providing the potential for probing the interiors of natural dynamos. As illustrated by linear theory, there are many different wave classes.

To obtain fundamental insights, we have paid particular attention to torsional Alfvén waves/oscillations and magnetic Rossby waves that can be excited in the geo- and jovian- dynamos. The two wave classes may be considered as typical modes occurring in magnetostrophic balance of rapidly rotating MHD fluids (Sect. 1.4). They may particularly be relevant for understanding the planetary magnetic variations, length-of-day variations, and possibly the surface appearance in gaseous planets. The observations enable the possible inference of the strength and its spatial structure of the poloidal field component within the dynamo region, and of the "hidden" toroidal component there. This will provide a crucial constraint on the dynamo theory at all.

Despite the sterling attempts of theoretical and computational scientists, we believe that there remain some unexplored issues and open questions, namely:

- The class of rotating MHD waves, whether MC or MAC, is clearly a zoo, exhibiting different dynamics and behaviours. Even the slow Rossby wave class appears to be distinct, dependent on the background magnetic field and the regime. We need a concrete catalogue to distinguish these modes and to elucidate their individual behaviours. This will enable the prediction of which waves best suit the inference of the quantity of interest within the dynamo.
- A mathematical challenge is to address the critical layers arising from the background magnetic field profile, the relevance of continuous spectra, and their potential feedbacks on the mean state; they were partly addressed (Acheson 1972; Nakashima 2020). Those concepts have been explored in the plasma phys-

ics and geophysical fluid dynamics, in which mean flows tend to be of primary interest. Their knowledge and techniques could hint at solutions in the current context.

- Is it possible to find waves that are topologically protected, such as those that have been found to exist in hydrodynamic rotating systems and plasmas (Delplace et al. 2017; Parker et al. 2020a, b)? If so, the edge waves could allow us to sense the vicinity of a boundary including a thin stably stratified layer.
- From an observational point of view, the existence of those waves and their characterisation are still a subject of debate. In particular, distinguishing a few candidate modes/branches from data seems to be a tricky issue. A methodology to separate individual waves has led to significant progress in Earth's seismology, and meteorology likely. Today's data-driven approaches might help to endorse this: they are now capable of extracting signals to incorporate the physics.
- Whereas wave motion could provide us the information about deep dynamos, do they play any roles in the dynamo action and the internal dynamics at all? There are classic ideas such as inertial wave generating helicity and thus a dynamo (Moffatt 1978; Davidson and Ranjan 2015) and the supression of zonal mean flows in the presence of magnetic field (Tobias et al. 2007). Furthermore, the interaction of waves with critical layers could lead to the driving of mean flows. It is uncertain how individual waves classes might feed dynamos. This would be another theoretical challenge for the future.

Appendix A Normal mode calculations

Normal mode solutions of torsional waves (5) and of magnetic Rossby waves (11) are computed individually, whilst considering a basic state in a spherical shell outside the tangent cylinder.

For normal mode solutions, e.g., $\langle \overline{u'_\phi} \rangle = \hat{u}_\phi(s) \exp \mathrm{i}\omega t$, the homogeneous part of (5) implies a second-order ODE with variable coefficients. This is an eigenvalue problem to determine the eigenfunction $\hat{u}_\phi$ with eigenvalue ω, given a basic state of U_A and $\langle \overline{\rho} \rangle$. Here we suppose a basic field, $U_A \propto (3/2) \cos \{ \pi(3/2 - 50s/19r_o) \} + 2$, which was adopted by Canet et al. (2014) to represent the 1d structure of the poloidal field part in the geodynamo (Gillet et al. 2010). The density $\overline{\rho}$ is assumed to be constant. We use the Matlab routine bvp4c to solve the eigenvalue problem in $0.35 \le s/r_o < 1$. The boundary conditions are $d\hat{u}_\phi/ds = 0$ at the inner boundary and $\hat{u}_\phi + (1 - s/r_o)d\hat{u}_\phi/ds = 0$ at $s/r_o = 0.99999$: the latter is introduced to avoid the numerical issue for singularities (Hori et al. 2020a). Figure A1a depicts profiles of eigenfunctions $\hat{u}_\phi$, for which a normalising factor is imposed at the inner bound. Their eigenvalues ω are listed in the legend in terms of dimensional periods $T = 2\pi/\omega$. For calculating the dimensional values we use $\rho = 1.13 \times 10^4 \, kg/m^3$, $r_o = r_{\mathrm{core}} = 3.485 \times 10^6 \, m$, and a factor of $1.12 \times 10^{-3} \, T$ for $\widetilde{\overline{B}_s}$, implying the maximal strength of the assumed backgound field is about 3.9 mT.

Similarly, the eigenvalue problem (11) for magnetic Rossby waves is solved for the eigenfunction $\hat{\psi}$ and the eigenvalue $\hat{\omega}$, given a basic state ω_M, β, and azimuthal
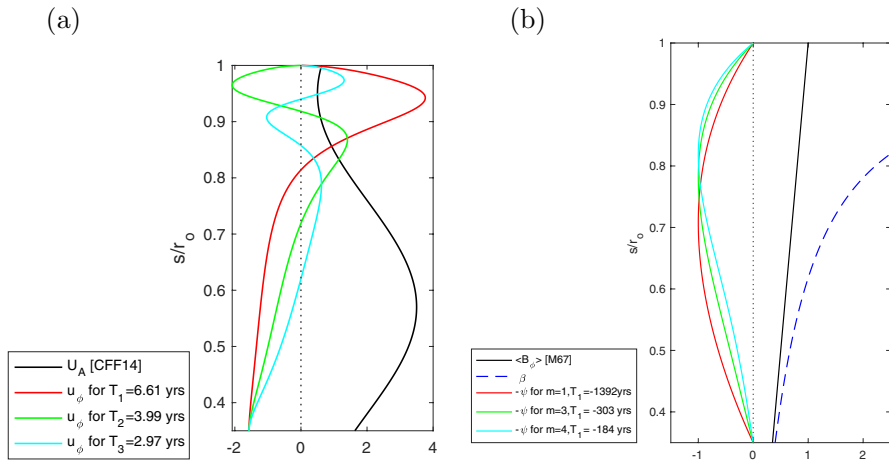
(a)

(b)

Fig. A1 **a** Normal modes of torsional oscillations (5). The black solid curve shows the normalised profile of the given background field U_A (Gillet et al. 2010; Canet et al. 2014). Other curves show the eigenfunctions $\hat{u}_\phi$ of the 1st (red), 2nd (green), and 3rd (cyan) normal modes. The eigenvalue of the i-th normal mode is listed in the legend, in which the period T_i is represented in years for a maximal background poloidal field 3.9 mT. **b** Normal modes of magnetic Rossby waves (11). The black solid and blue dashed curves show the normalised profiles of a background field $\langle \widetilde{B_\phi} \rangle$ (Malkus 1967) and beta parameter β, respectively. Other curves show the eigenfunctions $\hat{\psi}$ of the 1st normal mode for $m = 1$ (red), 3 (green), and 4 (cyan). For visualisation their profiles are presented in the negative domain, as $-\hat{\psi}$. Periods T_i of the i-th eigenvalue are represented in years, given a background toroidal field of maximal magnitude 13 mT

wavenumber m. We retain the constant density assumption, and assume a simple profile for the basic field, $\overline{\widetilde{B_\phi}} \propto s/r_o$ (Malkus 1967), since the structure of the toroidal field in the geodynamo is unknown. The beta parameter is given topographically (8), i.e., $\beta \propto s/(1 - s^2/r_o^2)$. The inner boundary condition is now $\hat{\psi} = 0$, while the modified condition is again adopted at the outer boundary. Figure A1b demonstrates the first normal modes for $m = 1, 3$, and 4. The eigenvalues are presented in the legend, where we suppose the dimensional quantities above and additionally $\Omega = 7.29 \times 10^{-5} \ s^{-1}$ and a maximal strength $\overline{\widetilde{B_\phi}}$ of 13 mT.

Appendix B WKBJ solutions

To gain insight of nonaxisymmetric wave motion (11), we suppose the coefficients slowly vary in s and seek a WKBJ solution. Rewriting the ODE as

$$\frac{d^2\hat{\psi}}{ds^2} + \frac{1}{s}\frac{d\hat{\psi}}{ds} + \lambda^2\hat{\psi} = 0 \qquad \text{where} \qquad \lambda^2 = \frac{\hat{\omega}\beta m}{(\hat{\omega}^2 - \omega_M^2)s} - \frac{m^2}{s^2}, \qquad (\text{B1})$$

we seek solutions in form of $\hat{\psi} = A(s) \exp i\theta(s)$. The ODE is then split into real and imaginary parts:

$$\frac{d^2A}{ds^2} - A\left(\frac{d\theta}{ds}\right)^2 + \lambda^2 A = 0 \quad \text{and} \quad \frac{d^2\theta}{ds^2} + \frac{2}{A}\frac{dA}{ds}\frac{d\theta}{ds} + \frac{1}{s}\frac{d\theta}{ds} = 0 , \quad \text{(B2)}$$

respectively. The amplitude is assumed to be slowly varying so that the highest order term of the real part is small, compared with other terms. Substituting this into the imaginary part gives

$$\frac{d^2\theta}{ds^2} = -\left(\frac{2}{A}\frac{dA}{ds} + \frac{1}{s}\right)\frac{d\theta}{ds} = -2s\left[\left(\frac{d\theta}{ds}\right)^2 - \lambda^2 + \frac{1}{2s^2}\right]\frac{d\theta}{ds} . \quad \text{(B3)}$$

If $d^2\theta/ds^2$ is also smaller than the other terms the equation is drastically simplified. Wave-like solutions then exist when $\lambda^2 > 1/2s^2$, leaving

$$A = \frac{A_0}{\sqrt{s}} \quad \text{and} \quad \left(\frac{d\theta}{ds}\right)^2 = \lambda^2 - \frac{1}{2s^2} . \quad \text{(B4)}$$

The local radial wavenumber $d\theta/ds$ (we denote as n) is determined by $\hat{\omega}$, β, m, s, and ω_{M}^2. The solutions become evanescent when $\lambda^2 < 1/2s^2$. Also it implies that the radial velocity, $\langle u'_s \rangle$, varies with $s^{-3/2}$.

Availability of data and materials All data appearing in Figs. 1, 2, 5, and 10 are publicly available.

Declarations

Conflict of interest There is no conflict of interest.

Code availability The codes used in this study are available upon request.

References

D.J. Acheson, J. Fluid Mech. **53**, 401–415 (1972)

D.J. Acheson, R. Hide, Rep. Prog. Phys. **36**, 159–221 (1973)

A. Antuñano et al., Astron. J. **158**, 130 (2019)

J. Aubert, C.C. Finlay, Nat. Geosci. **12**, 393–398 (2019)

J. Aubert, N. Gillet, Geophys. J. Int. **225**, 1854–1873 (2021)

J. Aubert, C.C. Finlay, A. Fournier, Nature **502**, 219–223 (2013)

J. Aubert, T. Gastine, A. Fournier, J. Fluid Mech. **813**, 558–593 (2017)

A.J. Biggin et al., Nature Geosci. **5**, 526–533 (2012)

J. Bloxham et al., J. Geophys. Res. Planets **127**, e2021JE007138 (2022)

S.J. Bolton et al., Space Sci. Rev. **213**, 5–37 (2017)

S.I. Braginsky, Geomagn. Aeron. **7**, 851–859 (1967)

S.I. Braginsky, Geomag. Aeron. **10**, 1–8 (1970)

S.I. Braginsky, P.H. Roberts, Geophys. Astrophys. Fluid Dyn. **79**, 1–97 (1995)

B. Buffett, Nature **507**, 484–487 (2014)

B. Buffett, H. Matsui, Geophys. J. Int. **218**, 1210–1225 (2019)

E.C. Bullard, C. Freedman, H. Gellman, J. Nixon, Phil. Trans. R. Soc. Lond. A **243**, 67–92 (1950)

F.H. Busse, J. Fluid Mech. **44**, 441–460 (1970)

F.H. Busse, Phys. Earth Planet. Int. **12**, 350–358 (1976)

F.H. Busse, J. Fluid Mech. **173**, 545–556 (1986)

F.H. Busse, R.D. Simitev, J. Fluid Mech. **751**, 216–227 (2014)

S.C. Cande, D.V. Kent, J. Geophys. Res. **100**, 6093–6095 (1995)

E. Canet, C.C. Finlay, A. Fournier, Phys. Earth Planet. Int. **229**, 1–15 (2014)

R. Chi-Durán, M.S. Avery, B.A. Buffett, Geophys. Res. Lett. **48**, e2021GRL094692 (2021)

U.R. Christensen, J. Wicht, in *Treatise on Geophysics,* 2nd edition, edited by G. Schubert, Vol.8, pp.245-277 (Elsevier, Oxford, 2015)

U.R. Christensen, J. Aubert, Geophys. J. Int. **166**, 97–114 (2006)

U.R. Christensen, P. Olson, Phys. Earth Planet. Int. **138**, 39–54 (2003)

A. Chulliat, P. Alken, S. Maus, Geophys. Res. Lett. **42**, 3321–3329 (2015)

J.E.P. Connerney, *et al.*, J. Geophys. Res. **127**, e2021JE007055 (2022)

V. Courtillot, J.L. Le Mouël, Nature **311**, 709–716 (1984)

P.A. Davidson, Geophys. J. Int. **195**, 67–74 (2013)

P.A. Davidson, A. Ranjan, Geophys. J. Int. **202**, 1646–1662 (2015)

C. Davies, C. Constable, Nat. Commun. **8**, 15593 (2017)

P. Delplace, J.B. Marston, A. Venaille, Science **358**, 1075–1077 (2017)

E. Dormy, J. Fluid Mech. **789**, 500–513 (2016)

E. Dormy, A.M. Soward, *Mathematical Aspects of Natural Dynamos* (CRC Press, Boca Raton, 2007)

C.C. Finlay, in *Dynamos,* Les Houches Session Roman88, edited by P. Cardin, L.F. Cugliandolo. pp. 403-450 (Elsevier, Amsterdam, 2008)

C.C. Finlay et al., Earth Planet. Sci. **72**, 156 (2020)

C.C. Finlay, A. Jackson, Science **300**, 2084–2086 (2003)

C.C. Finlay, M. Dumberry, A. Chulliat, M.A. Pais, Space Sci. Rev. **155**, 177–218 (2010)

L.N. Fletcher, Geophys. Res. Lett. **44**, 4725–4729 (2017)

A. Fournier, J. Aubert, E. Thébault, Geophys. J. Int. **186**, 118–136 (2011)

T. Gastine, M. Heimpel, J. Wicht, Phys. Earth Planet. Int. **232**, 36–50 (2014a)

T. Gastine, J. Wicht, L.D.V. Duarte, M. Heimpel, A. Becker, Geophys. Res. Lett. **41**, 5410–5419 (2014b)

F. Gerick, D. Jault, J. Noir, Geophys. Res. Lett. **48**, e2020GL090803 (2021)

N. Gillet et al., Proc. Nat. Acad. Sci. **119**, e2115258119 (2022)

N. Gillet, D. Jault, E. Canet, A. Fournier, Nature **465**, 74–77 (2010)

N. Gillet, D. Jault, E. Canet, Geophys. J. Int. **210**, 1503–1516 (2017)

N. Gillet, L. Huber, J. Aubert, Geophys. J. Int. **219**, 522–539 (2019)

G.A. Glatzmaier, P.H. Roberts, Nature **337**, 203–209 (1995)

G.A. Glatzmaier, M. Evonuk, T.M. Rogers, Geophys. Astrophys. Fluid Dyn. **103**, 31–51 (2009)

G. Hellio, N. Gillet, Geophys. J. Int. **214**, 1585–1607 (2018)

R. Hide, Phil. Trans. R. Soc. Lond. A **259**, 615–647 (1966)

C.A. Higgins, T.D. Carr, F. Reyes, Geophys. Res. Lett. **23**, 2653–2656 (1996)

R. Holme, in *Treatise on Geophysics,* 2nd edition, edited by G. Schubert, Vol. 8, pp. 91-113 (Elsevier, Oxford, 2015)

K. Hori, C.A. Jones, A. Antuñano, L.N. Fletcher, S.M. Tobias, Nat. Astron. in press. (2022)

K. Hori, S.M. Tobias, R.J. Teed, in *Proc. Japan Soc. Fluid Mech. Annual Meeting 2020*, 104 (2020b). arXiv:2009.13095 [physics.flu-dyn]

K. Hori, in *Proc. Japan Soc. Fluid Mech. Annual Meeting 2019*, 174 (2019)

K. Hori, S. Yoshida, Geophys. Astrophys. Fluid Dyn. **102**, 601–632 (2008)

K. Hori, S. Takehiro, H. Shimizu, Phys. Earth Planet. Int. **236**, 16–35 (2014)

K. Hori, C.A. Jones, R.J. Teed, Geophys. Res. Lett. **42**, 6622–6629 (2015)

K. Hori, R.J. Teed, C.A. Jones, Phys. Earth Planet. Int. **276**, 68–85 (2018)

K. Hori, R.J. Teed, C.A. Jones, Earth Planet. Sci. Lett. **519**, 50–60 (2019)

K. Hori, S.M. Tobias, C.A. Jones, J. Fluid Mech. **904**, R3 (2020a)

D. Jault, C.C. Finlay, in *Treatise on Geophysics,* 2nd edition, edited by G. Schubert, Vol.8, pp.225-244 (Elsevier, Oxford, 2015)

C.A. Jones, in *Treatise on Geophysics,* 2nd edition, edited by G. Schubert, Vol.8, pp.115-159 (Elsevier, Oxford, 2015)

C.A. Jones, Annu. Rev. Fluid Mech. **43**, 583–614 (2011)

C.A. Jones et al., Icarus **216**, 120–135 (2011)

C.A. Jones, Icarus **241**, 148–159 (2014)

C.A. Jones, R. Holme, Geophys. Res. Lett. **44**, 5355–5359 (2017)

C.A. Jones, K.M. Kuzanyan, R.H. Mitchell, J. Fluid Mech. **634**, 291–319 (2009)

A. Kageyama, T. Sato, Phys. Plasmas **2**, 1421–1431 (1995)

Y. Kaspi et al., Nature **555**, 223–226 (2018)

M. Kono, P.H. Roberts, Rev. Geophys. **40**, 4 (2002)

M. Korte, C. Constable, F. Donadini, R. Holme, Earth Planet. Sci. Lett. **312**, 497–505 (2011)

J.N. Kutz, S.L. Brunton, B.W. Brunton, J.L. Proctor, *Dynamic Mode Decomposition: Data-Driven Modeling of Complex Systems* (SIAM, Philadelphia, 2016)

B. Lehnert, Astrophys. J. **119**, 647–654 (1954)

P.W. Livermore, R. Hollerbach, C.C. Finlay, Nat. Geosci. **10**, 62–68 (2017)

S.D. London, Geophys. Astrophys. Fluid Dyn. **111**, 115–130 (2017)

M.S. Longuet-Higgins, Phil. Trans. R. Soc. Lond. A **262**, 511–607 (1968)

W.V.R. Malkus, J. Fluid Mech. **28**, 793–802 (1967)

M. Mandea et al., Space Sci. Rev. **155**, 147–175 (2010)

X. Márquez-Artavia, C.A. Jones, S.M. Tobias, Geophys. Astrophys. Fluid Dyn. **111**, 282–322 (2017)

H.K. Moffatt, *Magnetic Field Generation in Electrically Conducting Fluids* (Cambridge University Press, Cambridge, 1978)

K.M. Moore et al., Nat. Astron. **3**, 730–735 (2019)

R. Nakashima, PhD thesis, Kyushu University (2020)

A. Nilsson, R. Holme, M. Korte, N. Suttie, M. Hill, Geophys. J. Int. **198**, 229–248 (2014)

A. Nilsson, N. Suttie, M. Korte, R. Holme, M. Hill, Geophys. J. Int. **222**, 1423–1432 (2020)

A. Nilsson, N. Suttie, J.S. Stoner, R. Muscheler, Proc. Nat. Acad. Sci. **119**, e2200749119 (2022)

M.A. Pais, D. Jault, Geophys. J. Int. **173**, 421–443 (2008)

M.A. Pais, A.L. Morozova, N. Schaeffer, Geophys. J. Int. **200**, 402–420 (2015)

J.B. Parker, J.W. Burby, J.B. Marston, S.M. Tobias, Phys. Rev. Res. **2**, 033425 (2020b)

J.B. Parker, J.B. Marston, S.M. Tobias, Z. Zhu, Phys. Rev. Lett. **124**, 195001 (2020a)

L.G. Redekopp, J. Fluid Mech. **82**, 725–745 (1977)

V.A. Ridley, R. Holme, J. Geophys. Res. Planets **121**, 309–337 (2016)

P.H. Roberts, in *Lectures on Solar and Planetary Dynamos,* edited by M.R.E. Proctor, A.D. Gilbert, pp.1-58 (Cambridge University Press, Cambridge, 1994)

P.H. Roberts, J.M. Aurnou, Geophys. Astrophys. Fluid Dyn. **106**, 157–230 (2012)

Y. Sasaki, S. Takehiro, M. Ishiwatari, M. Yamada, Phys. Earth Planet. Int. **276**, 36–43 (2018)

N. Schaeffer, D. Jault, Geophys. Res. Lett. **43**, 4922–4928 (2016)

N. Schaeffer, D. Jault, H.-C. Nataf, A. Fournier, Geophys. J. Int. **211**, 1–29 (2017)

P.J. Schmid, J. Fluid Mech. **656**, 5–28 (2010)

G. Schubert, K.M. Soderlund, Phys. Earth Planet. Int. **187**, 92–108 (2011)

T. Schwaiger, T. Gastine, J. Aubert, Geophys. J. Int. **219**, S101–S114 (2019)

L. Silva, L. Jackson, J. Mound, J. Geophys. Res. **117**, B10101 (2012)

D.J. Stevenson, Space Sci. Rev. **152**, 651–664 (2010)

D.J. Stevenson, Annu. Rev. Earth Planet. Sci. **48**, 465–489 (2020)

J.A. Tarduno et al., Science **327**, 1238–1240 (2010)

J.B. Taylor, Proc. R. Soc. Lond. A **274**, 274–283 (1963)

R.J. Teed, C.A. Jones, S.M. Tobias, Geophys. J. Int. **196**, 724–735 (2014)

R.J. Teed, C.A. Jones, S.M. Tobias, Earth Planet. Sci. Lett. **419**, 22–31 (2015)

R.J. Teed, C.A. Jones, S.M. Tobias, Geophys. J. Int. **216**, 123–129 (2019)

S.M. Tobias, J. Fluid Mech. **912**, P1 (2021)

S.M. Tobias, P.H. Diamond, D.W. Hughes, Astrophys. J. **667**, L113–L116 (2007)

G.K. Vallis, *Atmospheric and Oceanic Fluid Dynamics*, 2nd edn. (Cambridge University Press, Cambridge, 2017)

J. Verhoeven, S. Stellmach, Icarus **237**, 143–158 (2014)

J. Wicht, U.R. Christensen, Geophys. J. Int. **181**, 1367–1380 (2010)

G.P. Williams, T. Yamagata, J. Atmos. Sci. **41**, 453–478 (1984)

R.K. Yadav, T. Gastine, U.R. Christensen, S.J. Wolk, K. Poppenhaeger, Proc. Nat. Acad. Sci. **113**, 12065–12070 (2016)

S. Zatman, J. Bloxham, Nature **388**, 760–763 (1997)